Railton, C. J. (2016). Rotated sub-grids in the FDTD Method. IEEE Transactions on Antennas and Propagation, 64(7), 3047-3054. DOI: 10.1109/TAP.2016.2559520

Peer reviewed version

Rotated sub-grids in the FDTD Method

Chris J. Railton, *Member, IEEE*

***Abstract*— Although the Finite Difference Time Domain (FDTD) method is well established for addressing a wide variety problems, a long standing challenge is to reduce discretization errors while avoiding the use of impractically large numbers of cells, particularly when the structure is large and contains regions of fine detail. One solution is to use sub-grids but in most published work, Cartesian sub-grids are proposed which are constrained to have the same orientation as the main grid. However there is considerable benefit to allowing for the sub-grid to be rotated. In this work, a method for introducing a rotated sub-grid into the FDTD mesh is presented and its effectiveness, accuracy and stability is demonstrated by means of some simple examples.**

***Index Terms*—FDTD methods**

I. INTRODUCTION

THE Finite Difference Time Domain (FDTD) method has been used to solve a wide variety of electromagnetic problems over a period of many decades. Nevertheless structures which contain fine geometrical detail and which are also electrically large still present a challenge. The difficulty is much greater for structures such as conformal antenna arrays in which different elements are orientated in different directions. An example of this is the system described in [1] which is a hemispherical array of slot antenna elements designed for use in a breast tumor detection system. In [2] and [3], a method is presented whereby each element of the array is modeled using a Cartesian mesh which is orientated in the most appropriate way for that element. The results were then rotated so that they matched the orientation of the element in the array. By means of a three stage process, the antenna array was characterized using computational resources which were several orders of magnitude smaller than would be needed if using direct FDTD methods.

Although good results were obtained, the approximation was made that energy was transferred only in one direction, ie. from the excited element to all the non-excited ones and multiple reflections were ignored. When the coupling between elements is small, as in the case of [1], this is appropriate. If the coupling is high, however, then a more rigorous approach is needed.

In the literature, a number of sub-gridding schemes have been proposed to address this type of problem, for instance [4][5] [6][7] but these have only been applied to situations where all the grids are orientated along the same Cartesian axes. For structures such as conformal antenna arrays, it would be preferable if sub-grids were orientated in the same directions as the elements such as in the situation shown in Figure 1. A scheme which does allow this in two dimensions is described in [8], however a constant time step is used throughout the problem space which leads to inefficiency when the sub-grid cell size is much smaller than the main grid size. A number of hybrid schemes have also been proposed in order to overcome the limitation to a fixed coordinate system, for instance the combination of FDTD with FEM [9], MoM [10], FVTD [11] and conformal FDTD [12] but there is very little in the literature concerning methods which allow several different FDTD grids to be combined.

In this contribution, the methods of [3], [6] and [13] are generalized and extended to allow application to sub-grids which are rotated with respect to the main grid and which account for the flow of energy in all directions. A preliminary outline of the approach is given in [14]. An added benefit of the proposed method is that the ratio of cell sizes in the main grid to those in the sub-grid is not restricted. In particular, unlike most sub-gridding schemes, this ratio does not need to be an integer.

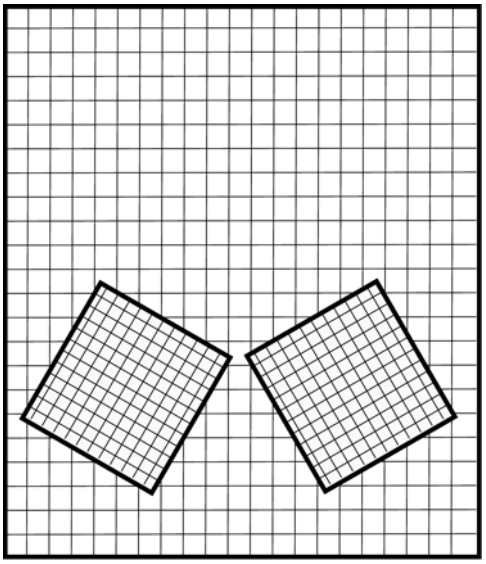

Figure 1 - Rotated sub-grids used to model tilted antenna elements.

II. THE ALGORITHM IN ONE DIMENSION

In order to set the scene, the proposed sub-gridding algorithm is first described for one dimensional problems then, in Section IV, the description is extended to full three dimensional situations.

Submitted for publication 2015.

C. J. Railton is a Professor Emeritus with the Electrical Engineering Department, University of Bristol, Bristol, UK . e-mail: chris.railton@bristol.ac.uk).

In one dimension, the problem to be solved is expressed as an array of staggered E and H nodes terminated at each end by a suitable boundary condition as shown in Figure 2. The E and H nodes are shown as circles and lines respectively. When sub-gridding is required, the system can be expressed as an equivalent problem which is illustrated in Figure 3. Here, following [6], the original array is retained but a second array is placed so that it overlaps, and extends beyond, the region in which the sub-grid is required. The node spacing of this second array may be chosen arbitrarily and independently of the node spacing of the main array. At each edge of the region where the sub-grid is required, two points are defined, labeled as IS and OS, which represent Huygens surfaces. These points are located half way between an E node and its neighboring H node in the sub-array. At points OS, the fields in the sub-array are expressed as equivalent currents which are used as sources in the main array. At points IS, the fields in the main array are expressed as equivalent currents which are used as sources in the sub-array. The arrows in Figure 3 indicate the direction of energy flow.

In the absence of discretization errors, the fields, sources and media outside the OS surface in the main array and inside IS in the sub-array, called the "working regions", as well as the gap between OS and IS are identical to those in the original problem [6]. The regions of the sub-array outside the surface OS and of the main array inside the surface IS are "non-working regions" and could in principle be removed. However for convenience, and to reduce numerical noise, they are retained. Similarly, the boundary conditions placed at the sub-array outer boundary can, in principle, be arbitrary but have been chosen to be absorbing in order to minimize numerical noise.

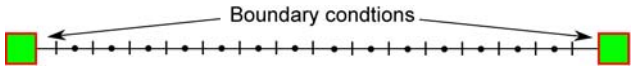

Figure 2 - The original problem in one dimension

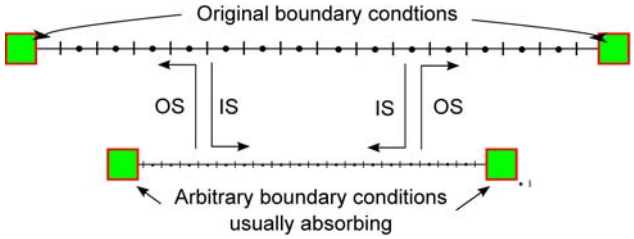

Figure 3 - The equivalent one dimensional problem

A more detailed picture of the way the Huygens surfaces are implemented is shown in Figure 4 and Figure 5. Unlike in [6], the node spacing and position of the sub-array is completely independent of those of the main array, hence all nodes are, in general, at different locations.

Taking the case of IS first, the Huygens surface is defined as being half way between E and H nodes of the sub-array as shown by the thick vertical line. In order to correctly apply the equivalent currents from the main array, the values of E and H in the main array need to be known at the positions of the E and H nodes in the sub-array. These values are obtained by linear interpolation in space. In Figure 4, the interpolated E node is shown as the empty circle and the arrows indicate the nodes used in the interpolation process. Similarly, the interpolated H node is shown as a grey vertical line.

For OS, the Huygens surface is again defined as being half way between E and H nodes of the sub-array as shown by the thick vertical line in Figure 5. To apply the equivalent currents to the main array, the process used is the reverse as that used for IS except that the source nodes which are used in the sub-grid are spaced by half the size of the main grid cell instead of using adjacent nodes. This modification has been found not to affect the accuracy but it improves the stability performance. The values of the equivalent currents in the main array are known at the positions of the E and H nodes in the sub-array, shown by the empty circle and grey vertical line in Figure 5. These currents are distributed to the neighboring E and H nodes using the same weightings as would be used for linear interpolation.

It is noted that in [6], only the H field in the main array requires interpolation in space because all the other required values are directly available due to the alignment of the main array and the sub-array. In the more general situation described in this paper, both E and H fields need to be interpolated.

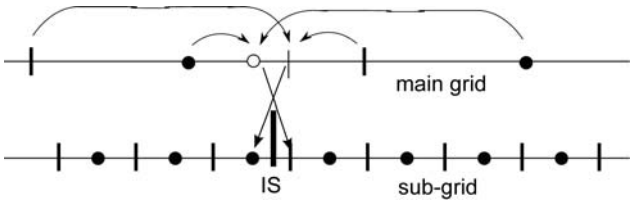

Figure 4 - Detail of the IS surface implementation

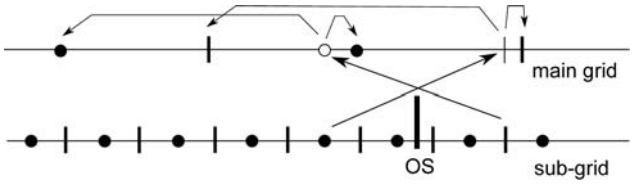

Figure 5 - Detail of the OS surface implementation

III. Stability Issues

The method as described exhibits a similar problem of late time instability to the one reported in [6] which was, in that case, mitigated using spatial filtering. It has been found that a similar approach is effective for the case of rotated sub-arrays presented in this contribution. To facilitate this, a "filtered array" is defined which has nodes at the same positions as the main array but only those which are required for interpolation are needed. The field value of each filtered node is calculated by taking a weighted sum of the corresponding main array value together with the values of its nearest neighbors as shown in Figure 6 and given in equation 1. For clarity, only the H field filtering is shown but an identical scheme is used for E fields. The filtered array values are then used for the spatial interpolation as before. In three dimensions, the weighted sum is taken with the 6 nearest neighbors using the template given in equation 2.

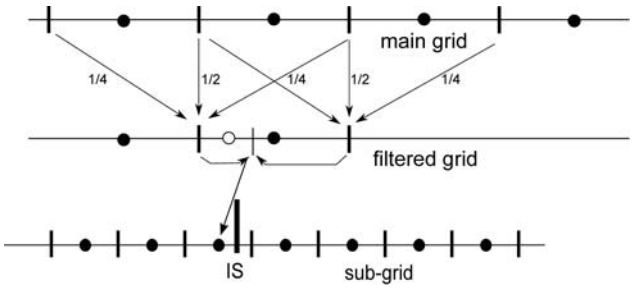

Figure 6 - Filtering scheme for H fields in one dimension

$$\overline{H}_i = \frac{H_{i-1}}{4} + \frac{H_i}{2} + \frac{H_{i+1}}{4} \tag{1}$$

$$\begin{aligned}\overline{H}_{i,j,k} = &\frac{H_{i-1,j,k}}{8} + \frac{H_{i,j-1,k}}{8} + \frac{H_{i,j,k-1}}{8} \\ &+ \frac{H_{i,j,k}}{4} \\ &+ \frac{H_{i+1,j,k}}{8} + \frac{H_{i,j+1,k}}{8} + \frac{H_{i,j,k+1}}{8}\end{aligned} \tag{2}$$

For distribution on OS, the opposite process is followed Instead of distributing the equivalent currents directly to the main array, as in Figure 5, they are first distributed to an "intermediate array" from where they are further distributed to the main array using the same weightings as used for filtering. This is shown in Figure 7. Results showing the effectiveness of this scheme are given in Section VII.

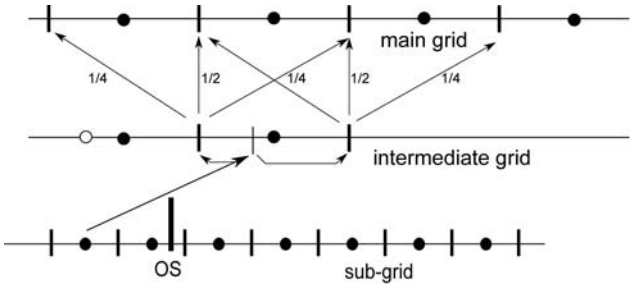

Figure 7 - Distribution to H field nodes in one dimension

IV. SUB-GRIDS ROTATED WITH RESPECT TO THE MAIN GRID AXES IN THREE DIMENSIONS

In three dimensions, OS and IS are cuboidal Huygens surfaces which are aligned with the sub-grid and may be rotated with respect to the main grid. This general situation is shown in Figure 8 where the inner cuboid is the surface IS and the outer cuboid is OS. A cross-section of the sub-grid is shown in Figure 9 with the two surfaces indicated. The outer boundary of the sub-grid corresponds to the two end points of the sub-array in Figure 3 and is terminated with an absorbing boundary.

The structure shown in Figure 8 and Figure 9 is set up in the following way:

i. Choose a cuboidal region in the computational domain in which the sub-grid is required. Call the bounding surface of this region the Inner Surface, IS. The orientation of this surface with respect to the main grid can be freely chosen. In Figure 8 it is shown to be rotated by an angle of 30^O.

ii. Define a second surface, the Outer Surface, OS, which surrounds the Inner Surface at a distance which is an integer multiple of the sub-grid cell size, usually chosen to be 9.

iii. Define a third surface, the sub-grid outer boundary, which surrounds the Outer Surface at a distance which is an integer multiple of the sub-grid cell size from the Outer Surface.

In Figure 10, which is an expanded view of the area shown in red in Figure 9, a more detailed view of the interface between the two grids can be seen. Only the relevant nodes close to the boundaries are shown. Energy is transferred between the two grids in the direction of the grey arrows by applying the equivalence principle. Fields impinging on the inner surface, IS, from the main grid are replaced by equivalent electric and magnetic currents which are used as excitation sources for the sub-grid.

Similarly the fields impinging on the outer surface, OS, from the sub-grid are replaced by equivalent electric and magnetic currents which are used as excitation sources for the main grid.

The key steps of the algorithm are summarized as follows. Details are given in the Section V.

i. At each coarse grid time step, the field values on the OS boundary nodes in the sub-grid are expressed as equivalent currents and these are distributed firstly to the intermediate grid nodes and thence to the surrounding main grid nodes and added to their update equations.

ii. At each sub-grid time step, the field values in the main grid are filtered and assigned to the filtered grid nodes. These values are then interpolated to the IS boundary nodes in the sub-grid. They are converted to equivalent currents which are added to the update equations for the sub-grid nodes. Since the time step in the coarse grid is larger than in the fine grid, interpolation in time is required in order to find the value of the main grid fields at each sub-grid time step.

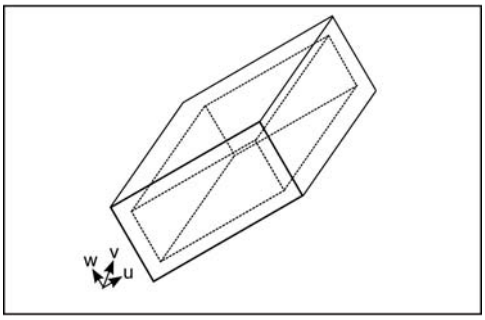

Figure 8 - A sub- grid rotated with respect to the main grid coordinate system showing the IS and OS surfaces.

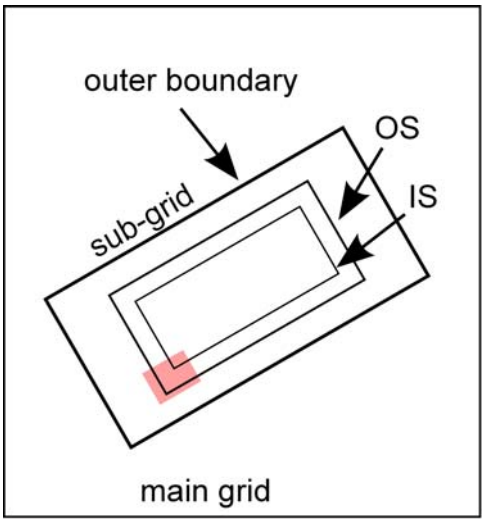

Figure 9 - Section through the rotated sub-grid showing boundary surfaces

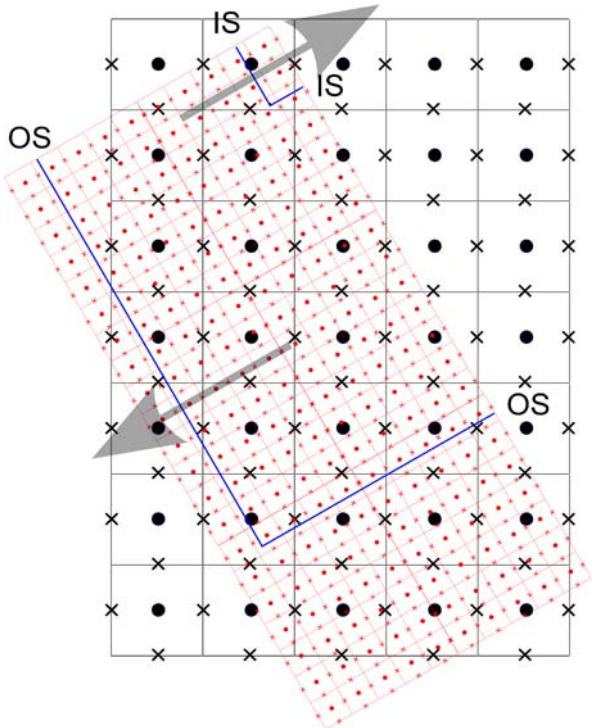

Figure 10 – Interface between tilted sub-grid and the main grid.

V. INTERFACE BETWEEN THE MAIN GRID AND THE SUB-GRID

A. The Inner surface - interpolation

For illustration, Figure 11 and Figure 12 show a portion of the $-\hat{u}$ boundary on the surface, IS. The surface itself is in between the rows of E and H field nodes which are shown in green. On this surface the fields in the main mesh are approximated by interpolation and represented as equivalent currents which are used as excitation sources for the sub-grid in the following way.

i. Referring to Figure 11, for the position of each H node on IS in the sub-grid, shown as a green circle, the value of **H** in the main grid is found from the surrounding H_x, H_y and H_z nodes using linear interpolation. Each field component is individually interpolated from eight surrounding nodes to approximate the full **H** vector at that point. The arrows show one of the target nodes in the sub-grid and some of the main grid nodes from which the field values are interpolated.

ii. The amplitudes of the equivalent current at these nodes are found using $J = -\hat{u} \times H$.

iii. The J vector, which, at this stage, is still expressed in (x,y,z) components, is rotated to obtain the (u,v,w) components.

iv. The E_v or E_w sub-grid field amplitude is updated using Maxwell's equation $\dot{\underline{E}} = \varepsilon^{-1} \underline{J}$. The contribution of curl H to this equation will have already been included using the usual FDTD update equations. The contributions of these currents are added to the update equations for the E nodes in the sub-grid which are half a cell size in the direction of the inward normal to the surface as shown by the blue arrow.

For example, if the cell containing the target H node has the index (p,q,r) then the update equation for the affected E_v node is given by equation 3 where δu,δv,δw,δt are the sub-grid cell sizes and time step respectively.

$$E^{n+1}_{v(p+1,q,r)} = E^{n}_{v(p+1,q,r)} - \frac{\delta t}{\varepsilon \delta u}\left(H^{n+0.5}_{w(p+1,q,r)} - H^{n+0.5}_{w(p,q,r)}\right) + \frac{\delta t}{\varepsilon \delta v}\left(H^{n+0.5}_{u(p,q,r+1)} - H^{n+0.5}_{u(p,q,r)}\right) - \frac{\delta t}{\varepsilon} \underline{J^{n+0.5}_{(p,q,r)}} \cdot \underline{\hat{v}} \quad (3)$$

v. Referring to Figure 12, for each E node on IS in the sub-grid, shown as a green cross, the value of **E** in the main grid is found from the surrounding E_x, E_y and E_z nodes using linear interpolation in the same way as described for the H field.

vi. The amplitudes of the equivalent current are found at these nodes using $M = \hat{u} \times E$.

vii. The M vector, which, at this stage, is still expressed in (x,y,z) components, is rotated to obtain the (u,v,w) components.

viii. The H_v or H_w sub-grid field amplitude is updated using Maxwell's equation $\dot{\underline{H}} = \mu^{-1}\underline{M}$. The contribution of curl H to this equation will have already been included using the usual FDTD update equations. The contributions of these currents are added to the update equations for the H nodes in the sub-grid which are half a cell size in the direction of the outward normal to the surface as shown by the blue arrow.

For example, if the cell containing the target E node has index (p+1,q,r) then the update equation for the affected H_w node is given by equation 4.

$$H^{n+0.5}_{w(p,q,r)} = H^{n-0.5}_{w(p,q,r)} + \frac{\delta t}{\mu \delta u}\left(E^{n}_{u(p,q+1,r)} - E^{n}_{u(p,q,r)}\right) - \frac{\delta t}{\mu \delta v}\left(E^{n}_{v(p+1,q,r)} - E^{n}_{v(p,q,r)}\right) - \frac{\delta t}{\mu}\underline{M^{n}_{(p+1,q,r)}} \cdot \hat{\underline{w}} \qquad (4)$$

B. The Outer surface - distribution

Figure 13 and Figure 14 shows a portion of the surface, OS. On this surface the fields in the sub-grid are represented as equivalent currents which are used as excitation sources for the main grid in the following way.

i. Referring to Figure 13, for each H node on OS in the sub-grid, shown as green circles, the value of the equivalent current, J, is found using $J = -\hat{u} \times H$.

ii. This current is shared out to the surrounding H nodes in the main grid using the same weightings as were used for the inner surface interpolation. The arrows show one of the source sub-grid nodes and the target main grid nodes.

iii. The contributions of these currents are added to the update equations for the E nodes in the main grid which are half a main grid cell size towards the sub-grid as shown by the blue arrows.

iv. Referring to Figure 14, for each E node on OS in the sub-grid, the value of the equivalent currents, M are found using $M = \hat{u} \times E$.

v. This current is shared out to the surrounding E nodes in the main grid using the same weightings as would be used for linear interpolation.

vi. These contributions of these currents are added to the update equations for the H nodes in the main grid which are half a main grid cell size away from the sub-grid.

As in [6], interpolation in time as well as space is necessary at each iteration and, in order to do this correctly, the nodes near the boundary need to be advanced in time before those in the rest of the mesh. These precursors are calculated in a way analogous to [6] but because the two grids are not aligned, all the nodes which are required for the E and H field interpolations need to be advanced.

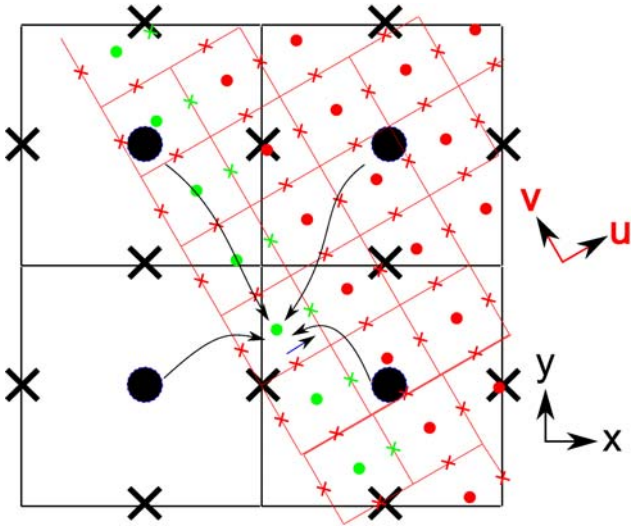

Figure 11 - Detail of H field interpolation

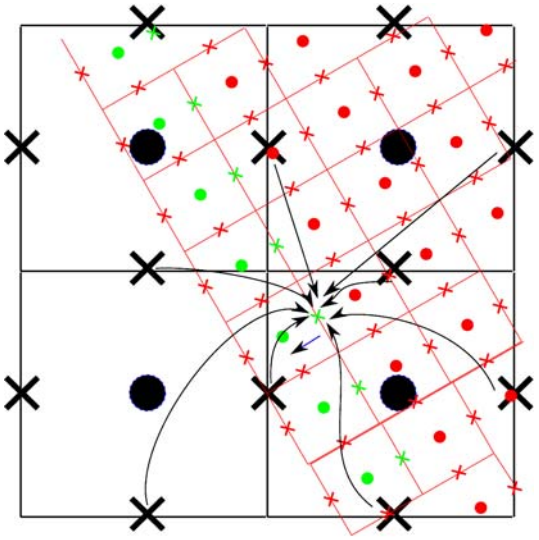

Figure 12 - Detail of E field interpolation

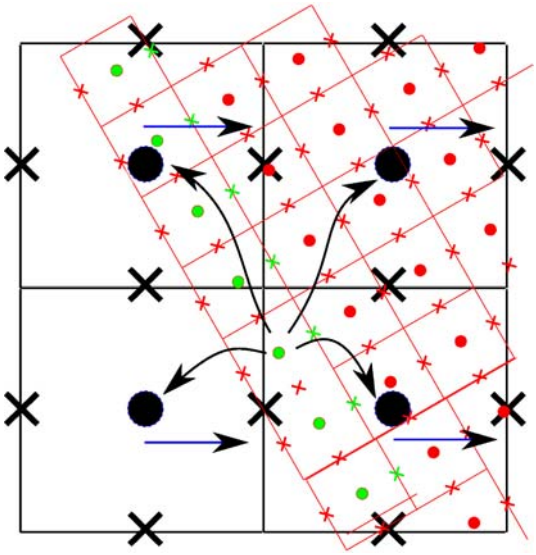

Figure 13 - Detail of H field distribution

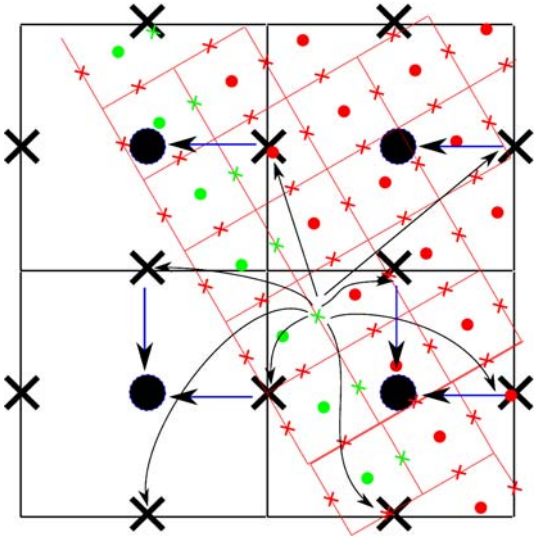

Figure 14 - Detail of E field distribution.

VI. Results

A. *Plane wave propagation through the sub-grid*

As a first test in order to demonstrate that waves will propagate through a sub-grid region without undue distortion or reflection, the arrangements shown in Figure 15a and Figure 16a were set up. Here there is a main grid, of size (1500,375,375)mm, which is excited by a plane wave pulse of width 439ps, having a peak frequency of 2.3GHz and corresponding to 80 main grid time steps, propagating from left to right. Within the main grid, a sub-grid having a size of (300,75,75)mm is placed and centered at coordinates (450,186,186). The cell size for the main grid was 3mm and for the sub-grid was 1mm. Probes were placed in the main grid at positions of 150mm, 185mm, 700mm and 750mm from the left hand boundary and in the sub-grid at positions of 350mm, 450mm and 550mm from the left hand boundary of the main grid. The positions of the probes are shown in the figures and these allow the pulse to be tracked as it propagates. The probes in the main grid are shown in red those in the sub-grid are shown in green.

Figure 15 shows the results for the case where the sub-grid is not rotated and Figure 16 shows the results for the case where the sub-grid is rotated by 30^{O} with respect to the main grid. In each case it can be seen that the pulse propagates with little distortion.

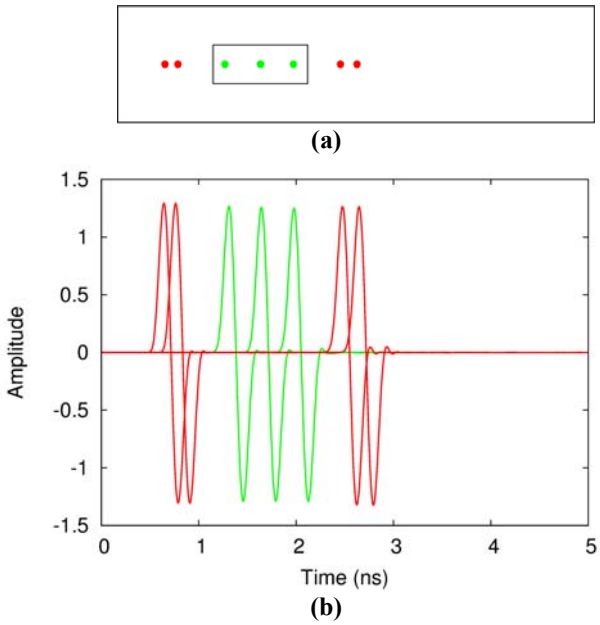

Figure 15 - Propagation through an unrotated sub-grid

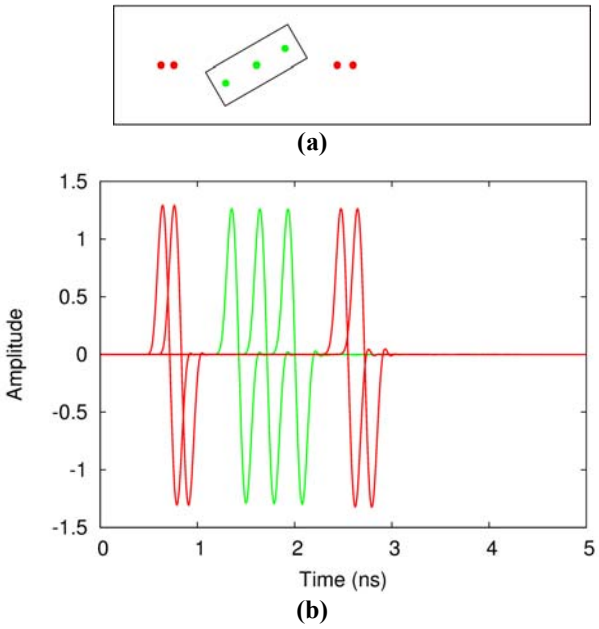

Figure 16 - Propagation through a rotated sub-grid

In order to ascertain the amount of reflection from the sub-grid region, the ratio of the incident and reflected pulse at the position of the left hand main grid probe was calculated. The results for various angles of rotation and a frequency up to 5GHz, corresponding to λ/20 in the main grid, is shown in Figure 17. Here it can be seen that the reflection is less than -50dB over almost all of the frequency range and angles of rotation. Results were also obtained using a sub-grid cell size of 0.6mm and, again, reflection levels better than -50dB were observed.

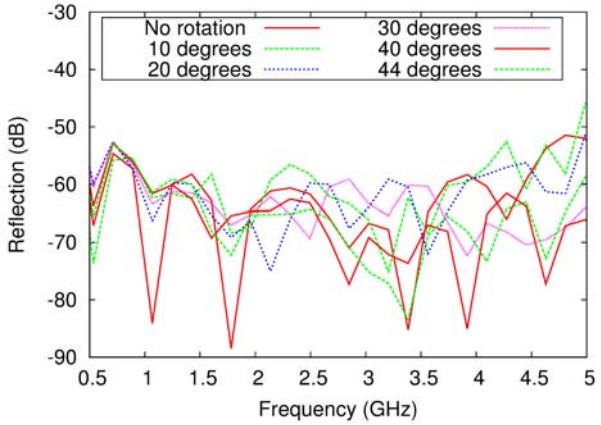

Figure 17 - Reflection from sub-grids rotated by various angles

B. Resonance frequency of a rotated resonant cavity

As a second example, the resonance frequency of a rectangular cavity which is rotated with respect to the main grid was calculated.

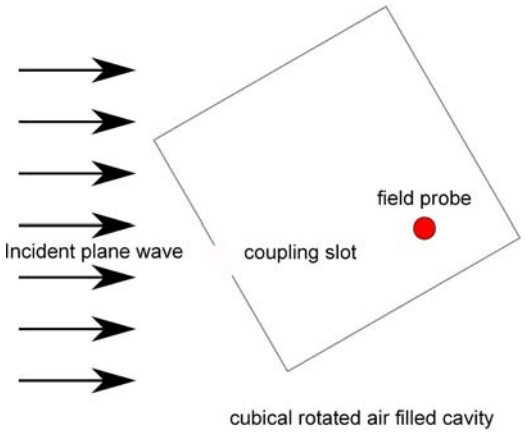

Figure 18 - Rotated air-filled resonant cavity

The cavity, shown in Figure 18, has a slot on one face through which energy from an incident plane wave is coupled in. In Figure 19 and Figure 20 the spectra of the field at the probe point are shown for various angles of rotation.

The size of the cavity is 20x20x20mm which has a lowest resonance frequency of 10.61GHz. It is placed in a sub-grid having dimensions of 99x25x25mm and the size of the main grid was 510x125x125mm. The cell size in the main grid was 3mm and in the sub-grid was 1mm.The structure was excited with a plane wave pulse having a width of 165ps and the field inside the cavity was probed at the position of the red circle. The position of the probe is arbitrary so long as nulls in the dominant mode are avoided. By taking the Fourier Transform of the field values, the calculated resonant frequency is obtained.

Figure 19 shows the results where rotated sub-grids are used and, for comparison, the corresponding results for a uniform mesh having a cell size of 1mm are shown in Figure 20. It can be seen that, for a uniform mesh the calculated frequency is not correct if the cavity is rotated, whereas when the rotated sub-grid is used, the results are consistent and accurate.

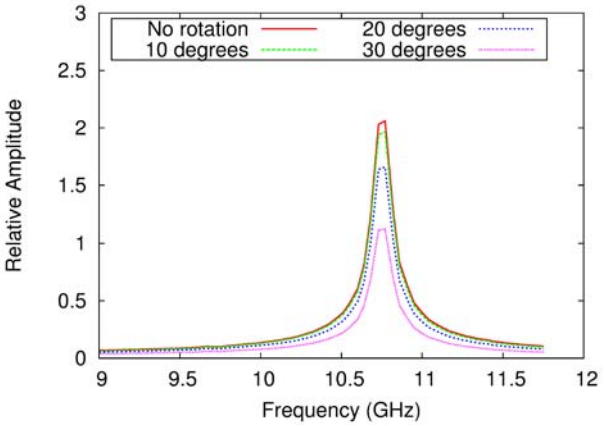

Figure 19 - Spectrum of the field inside the cavity calculated using a rotated sub-grid.

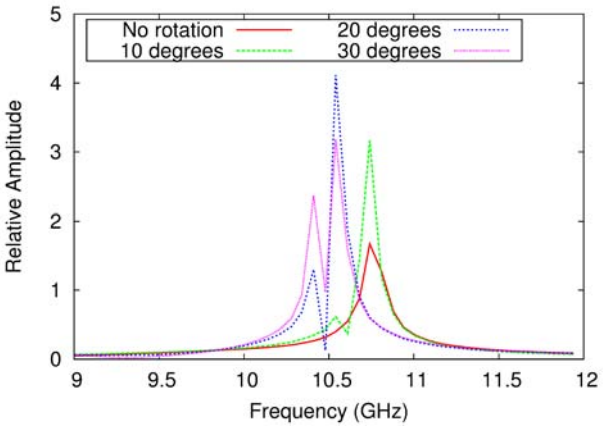

Figure 20 - Spectrum of the field inside the cavity calculated using a uniform mesh.

VII. Stability Checks

As stated in Section III, the basic method exhibits stability problems and filtering is introduced in order to mitigate these. A test case, similar to the scenario shown in Figure 16, was run until instability became apparent in order to see the effectiveness of the filtering. The results are shown in Figure 21 - Figure 24 for the cases of an unrotated sub-grid and a sub-grid which is rotated by 30^{O} with respect to the main grid.

Here it can be seen that without filtering, instability appears after approximately 15ns whereas, when filtering is used, instability only starts to appear after approximately 220ns, or

40,000 main grid iterations, which allows results to be obtained for many realistic problems. Similar behavior was observed for other angles of rotation.

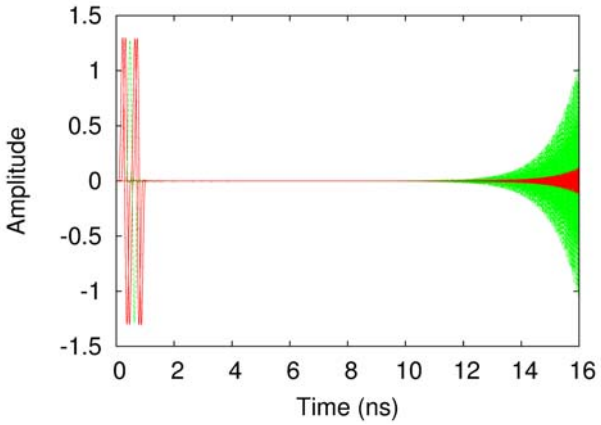

Figure 21 - Unrotated mesh unfiltered.

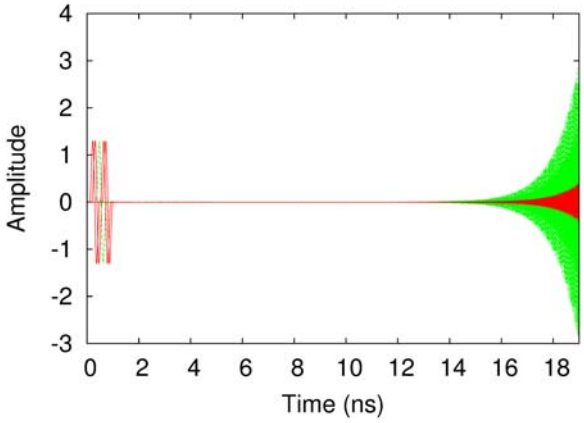

Figure 22 - 30 degree rotated mesh unfiltered.

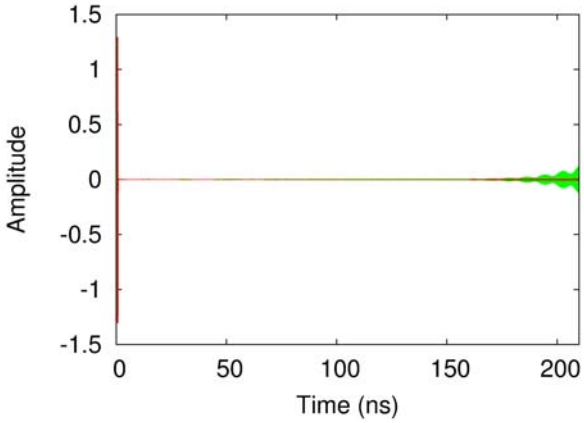

Figure 23 - Unrotated mesh filtered.

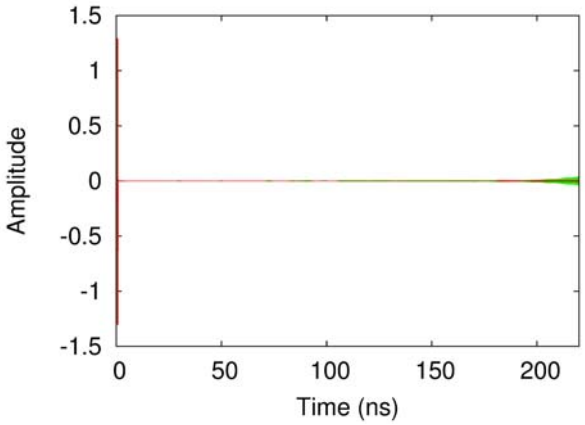

Figure 24 - 30 degree rotated mesh filtered.

VIII. Conclusions

In this contribution, a novel method for implementing rotated sub-grids in the FDTD method has been described and results presented which show that the method is effective. This method shows considerable promise and lends itself to being generalized to the use of rotated Cartesian sub-grids which have non-uniform cell sizes or to sub-grids with different coordinate systems, such as spherical or cylindrical coordinates. This would allow the efficient analysis of large, complicated and more realistic problems such as described in [1] and [3].

References

[1] M. Klemm, J. Leendertz, D. Gibbins, I.J. Craddock, A. Preece, R. Benjamin, “Towards Contrast Enhanced Breast Imaging using Ultra-Wideband Microwave Radar System” , Radio and Wireless Symposium (RWS), 2010, pp. 516-519

[2] Sema Dumanli and Chris Railton, “Analysis of coupled tilted slot antennas in FDTD using a novel Time Domain Huygens method with application to Body Area Networks”, IEEE Transactions on Antennas and Propagation, Vol. 60, No. 4, April 2012, pp 1987-1994.

[3] C Christodoulou, C. J. Railton, M. Klemm, D. Gibbins, I. J. Craddock, “Analysis of a UWB hemispherical antenna array in FDTD with a Time Domain Huygens method”, IEEE Trans. On Antennas and Propagation, Vol. 60, No. 11, Nov. 2012, pp 5251-5258.

[4] M. Okeniewski, E. Okoniewska and M. Stuchly, "Three dimensional subgridding algorithm for FDTD", IEEE Transactions on Antennas and Propagation, Vol 45, No. 3, March 1997, pp 422-429

[5] P. Thoma and T. Weiland, “A consistent subgridding scheme for the finite difference time domain method,” Int. J. Num. Model.: Electron. Network, Devices Fields, vol. 9, pp. 359–374, 1996.

[6] Jean-Pierre Bérenger, “The Huygens subgridding for the numerical solution of the Maxwell equations”, Journal of Computational Physics, 230 (2011) pp. 5635-5659.

[7] Oliver Podebrad, Markus Clemens and Thomas Weiland, "New Flexible Subgridding Scheme for the Finite Integration Technique", IEEE Trans. Magnetics, Vol. 39, No. 3, May 2003, pp. 1662-1665.

[8] Burkay Donderici and Fernando L. Teixeira, "Accurate Interfacing of Heterogeneous Structured FDTD Grid Components", IEEE Transactions on Antennas and Propagation, Vol 54, No. 6, June 2006, pp 1826-1835.

[9] Bao Zhu, Jiefu Chen, Wanxie Zhong, Qing Huo Liu, " A hybrid FETD-FDTD method with nonconforming meshes", Commun. Comput. Phys. Vol. 9, No. 3, March 2011, pp828-842

[10] A. Noga, T. Topa, and D. Wojcik, "Analysis of Complex Radiating Structures by Hybrid FDTD/MoM-PO Method", PIERS Online, Vol. 5, No. 8, 2009, pp 711-715

[11] Z.-L. He , K. Huang, and C.-H. Liang, "Hybrid Finite Difference/Finite Volume Method for 3-D Conducting Media Problems", PIERS M, Vol. 24, 85–95, 2012, pp 85-95.

[12] K. S. Yee, J. S. Chen, and A. H. Chang,“Conformal finite-difference time-domain (FDTD) with overlapping grids,” IEEE Trans. Antennas Propag., vol. 40, no. 9, pp. 1068–1075, Sep. 1992.

[13] Chris. J. Railton, “A Tilted Subgrid for Two Dimensional FDTD”, EuCAP 2015, Lisbon, Portugal.

[14] Chris. J. Railton, "A rotated subgrid for 3D FDTD", IEEE International Symposium on Antennas and Propagation & USNC/URSI National Radio Science Meeting, Vancouver, 2015, pp330-331.

Chris Railton received the BSc degree in Physics with Electronics from the University of London in 1974 and the PhD degree in Electronic Engineering from the University of Bath in 1988. During the period 1974-1984 he worked in the scientific civil service on a number or research and development projects in the areas of communications, signal processing and EMC. Between 1984 and 1987 he worked at the University of Bath on the mathematical modelling of boxed microstrip circuits. From 1987 until 2015 he worked in the Centre for Communications Research at the University of Bristol where he was engaged in research in the development of new algorithms for electromagnetic analysis, especially those related to the Finite Difference Time Domain method. Dr. Railton retired in 2015 and is now an Emeritus Professor at the University of Bristol.